Materials Advances

ROYAL SOCIETY OF CHEMISTRY

PAPER

View Article Online
View Journal | View Issue

Cite this: *Mater. Adv.*, 2023, 4, 3583

A PLA-tPU based magnesium ion incorporated CSH/nHA bioactive porous composite scaffold for critical bone defect repair

Zhi Shi,†[a] Guobin Huang,†[b] Zhongming Li,[c] Zhenkai Lou,[a] Zhiqiang Gong,[a] Xin Wang,[d] Chengyong Li*[d] and Bing Wang *[a]

The treatment of critical bone defects remains a significant challenge for advanced medicine. Chitosan/nano-hydroxyapatite (CS/nHA) composites have been widely developed in bone tissue engineering because of their attractive bioactivities. It has been demonstrated that incorporating a suitable amount of magnesium (Mg) into composite scaffolds can enhance the osteogenic effect. In this work, a series of bioactive porous composite scaffolds were prepared with polylactic acid (PLA), thermoplastic polyurethane (tPU), chitosan hydrochloride (CSH), nano-hydroxyapatite (nHA), and magnesium chloride ($MgCl_2$) mixed by freeze-drying technology, namely, PLA/tPU-1Mg-CSH/nHA (PT-1M-CN), PLA/tPU-1.5Mg-CSH/nHA (PT-1.5M-CN), PLA/tPU-1.75Mg-CSH/nHA (PT-1.75M-CN), and PLA/tPU-2Mg-CSH/nHA (PT-2M-CN). Characterization analysis shows that the scaffold's surrounding structure is similar to cancellous bone, which may be suitable for bone defect filling. *In vitro* biological experiments indicated that all the scaffolds had good biocompatibility, promoting rat bone marrow mesenchymal stem cell (rBMSC) proliferation, migration and osteogenic differentiation. Furthermore, the *in vivo* studies suggested that the scaffolds played a specific "bridge" role in the interconnection of osteoblasts which enhanced bone regeneration. By contrast, all the findings showed that the PT-1.75M-CN scaffold had the strongest osteogenic ability. Therefore, because of the superiorities of rich raw materials, simple preparation methods, and easy mass production, the PT-1.75M-CN scaffold provides a promising strategy for developing and promoting bone regeneration and tissue engineering applications.

Received 6th March 2023,
Accepted 29th June 2023

DOI: 10.1039/d3ma00109a

rsc.li/materials-advances

1. Introduction

Bones are among the most important organs in the human body, seriously affecting a patient's quality of life when damaged. Generally speaking, smaller bone defects are self-healing, while larger defects can only be repaired by additional graft filling.[1–3] Although autologous bone is still regarded as the gold standard of bone implants, its clinical application has impediments such as limited sources, difficult shape or size matching, and possible donor site infection.[4] Bone tissue engineering to find suitable bone substitutes has emerged in recent years. These substitutes consist of seed cells, scaffold materials and inducers, among which the scaffold materials are the most important component.[5]

Bone is a complex composed of organic and inorganic components. Composite organic and inorganic materials as bone substitute materials present a very promising strategy to simulate the composition of bone tissue.[6] As the main inorganic component of bone, hydroxyapatite (HA), has good biocompatibility and bone conductivity.[7,8] In addition, studies have shown that nano-hydroxyapatite (nHA) can promote cell osteogenic differentiation, with some advantages compared with HA.[9–12]

Chitosan (CS) is an organic material formed by the deacetylation of chitin and is common in nature.[13] Because of its good biological activity, degradability, and compatibility, CS is widely used in tissue engineering, especially in drug carriers, skin tissue engineering, and bone tissue engineering.[14–16] The composite material composed of CS and nHA can not only simulate

[a] *Department of Orthopedics, First Affiliated Hospital of Kunming Medical University, Kunming Medical University, Kunming, Yunnan, 650032, P. R. China. E-mail: drbingwang@163.com*
[b] *Yunnan Key Laboratory of Stomatology and Department of Dental Research, The Affiliated Stomatology Hospital of Kunming Medical University, Kunming, Yunnan 650500, P. R. China*
[c] *Yunnan Provincial Key Laboratory of Energy Saving in Phosphorus Chemical Engineering and New Phosphorus Materials The Higher Educational Key Laboratory for Phosphorus Chemical Engineering of Yunnan Province Faculty of Chemical Engineering Kunming University of Science and Technology, Kunming, Yunnan, 650500, P. R. China*
[d] *Spinal Surgery, The Affiliated Hospital of Yunnan University, Yunnan University, Kunming, Yunnan, 650021, P. R. China. E-mail: lichengyonglcy666@163.com*
† These authors contributed equally to this work.

the natural bone tissue composition, but also promote the osteogenic differentiation of cells, induce *in vivo* osteogenesis and regulate the inflammatory response of the implant site.[12,17,18]

However, some shortcomings have limited the application of CS/nHA composite materials in bone tissue engineering. On the one hand, CS is insoluble in water, so the application complexity caused by this feature must be solved.[19] On the other hand, the CS/nHA composite scaffold's mechanical strength is insufficient. Chitosan hydrochloride (CSH), having strong cationic properties and good water solubility while retaining the advantages of CS, is a good alternative to CS.[13,20,21] In addition, polylactic acid/thermoplastic polyurethane (PLA–tPU) blends can be mixed in different proportions to effectively improve the mechanical properties of tissue engineering scaffolds by combining the hardness of PLA and the toughness of tPU.[22]

Osteogenic activity is indispensable for the design of bone repair materials.[23] Magnesium ions (Mg^{2+}) found in bones are an essential component of the human body and play a vital role in human growth and development.[24,25] Furthermore, the function of Mg^{2+} in bone metabolism is encouraging.[26–28] It can regulate the activity of osteoblasts and osteoclasts and plays an important role in maintaining the homeostasis balance of the bone microenvironment.[29] In recent years, significant effort has been devoted to adding Mg^{2+} into scaffolds to enhance the proliferation, differentiation, and regeneration of bone cells.[30–34] In addition, Mg^{2+} can also induce macrophages to polarize by inhibiting the NF-κB pathway to produce an anti-inflammatory effect, which is further conducive to the migration and osteogenic differentiation of mesenchymal stem cells.[35,36] Vascular ingrowth is the premise of bone regeneration. On the one hand, the porosity of bone repair materials is conducive to forming a vascular network, further promoting new bone formation.[6,37,38] On the other hand, Mg^{2+} can stimulate the production of reactive oxygen species and induce the up-regulation of vascular endothelial growth factor expression in endothelial cells, thus promoting angiogenesis.[39,40] Considering that Mg^{2+} has the advantages of jointly promoting osteogenesis, angiogenesis and immune regulation, the incorporation of magnesium into the scaffold is expected to improve the osteogenic activity of bone implant materials.

Present preparation methods for porous scaffolds mainly include the salting-out, gas-foaming, thermally-induced phase separation, additive manufacturing, electrostatic spinning, and freeze-drying methods. Compared with other preparation methods, the freeze-drying method has a simple preparation process, does not affect the biological activity of the raw materials, and produces a scaffold with high porosity, which is cross-linked to form three-dimensional pores.[41] This study utilizes CSH/nHA as a bone component simulation, PLA/tPU as a framework, CS as the main force to create pores, and Mg^{2+} as an osteogenic active factor to develop a series of bioactive porous scaffolds using freeze-drying technology for repairing critical bone defects (Scheme 1). Subsequently, the mechanical properties and hydrophilicity of the bioactive porous scaffolds were explored. *In vitro* biological performance was investigated using rat bone marrow mesenchymal stem cells (rBMSCs). Finally, the effect of *in vivo* bone defect repair was assessed in a skull-critical bone defect model of Sprague-Dawley (SD) rats.

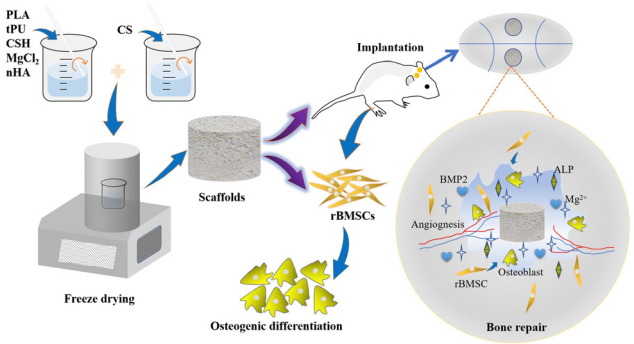

Scheme 1 Preparation of the PT-M-CN bioactive porous scaffold and its effect on bone regeneration.

2. Materials and methods

2.1. Materials

Polylactic acid (PLA) was purchased from NatureWorks (USA) and thermoplastic polyurethane (tPU) was purchased from Bayer (Germany). High-density chitosan, chitosan hydrochloride (CSH), and magnesium chloride ($MgCl_2$) were purchased from Macklin Biochemical Technology Co., Ltd (Shanghai, China). Nano-hydroxyapatite (nHA) was obtained from Hualan Chemical Technology Co., Ltd (Shanghai, China).

2.2. Preparation and characterization of scaffolds

tPU and PLA in a 1 : 3 mass ratio were first dissolved in *N*, *N*-dimethylformamide and dichloromethane respectively. After complete dissolution, they were mixed to obtain PLA–tPU blends. The high-density chitosan powder was dissolved in an acetic acid solution. Next, CSH, $MgCl_2$, and nHA were added to dichloromethane at different mass ratios of 6 : 1 : 2, 6 : 1.5 : 2, 6 : 1.75 : 2, and 6 : 2 : 2. After being stirred and dispersed evenly, they were placed in a super-high-speed homogenizer. Following uniform dispersion at 6000 rpm, they were added to the PLA-tPU blends, and the mixed liquid was poured into a mold with high-density chitosan solution for pore formation. Finally, bioactive porous composites PLA/tPU-1Mg-CSH/nHA (PT-1M-CN), PLA/tPU-1.5Mg-CSH/nHA (PT-1.5M-CN), PLA/tPU-1.75Mg-CSH/nHA (PT-1.75M-CN), and PLA/tPU-2Mg-CSH/nHA (PT-2M-CN) were obtained by processing at −80 °C in a vacuum freeze dryer.

The microstructures of the scaffold surfaces were observed by scanning electron microscopy (SEM, ZEISS, Germany). An energy dispersive spectrometer (EDS, Bruker, Germany) was used to observe the distribution of the components on the surface of the scaffolds. The mechanical strengths of the scaffolds were tested using a 1000 N force by a universal testing machine (Elecall, China), and the results were plotted as stress–strain curves. The pore structure of the scaffolds, including porosity, median pore diameter, and bulk density, were

characterized by mercury intrusion porosimetry. Scaffold water contact angles were detected with a contact angle measuring instrument (Bolaide, BLD-D1, China).

The scaffold extract was prepared with PBS solution at a ratio of 0.1 g mL^{-1} (ISO 10993-12 standard) to detect the sustained release of Mg^{2+} *in vitro*. After soaking for 1, 3, 7, 14, and 21 days, the scaffold extract was used to measure the Mg^{2+} concentration by inductively-coupled plasma-optical emission spectrometry (ICP-OES, PerkinElmer, USA).

2.3. *In vitro* cell experiments

2.3.1. Preparation of scaffold extract. All scaffolds were sterilized by γ-irradiation. Dulbecco's modified Eagle's medium (DMEM, Gibco, USA) containing 10% fetal bovine serum (FBS, Gibco, USA) and 1% penicillin–streptomycin (PS, Gibco, USA) was the basic cell medium in this study. Each scaffold was immersed individually at 37 °C for 24 h (0.1g scaffold: 1 ml basic medium (ISO 10993-12 standard)) to make the cell culture extract, and the osteogenic induction medium was added if necessary.

2.3.2. Isolation and culture of rat bone marrow mesenchymal stem cells (rBMSCs). Sprague-Dawley (SD) rats (4–6 weeks old) were purchased from the Laboratory Animal Department of Kunming Medical University. The rats were killed by cervical dislocation, and the femurs and tibias were extracted. Next, the bone marrow cavity was washed using the alpha-modified minimum essential medium (a-MEM, HyClone, USA) containing 10% FBS and 1% PS. The extracted rBMSCs were placed in an incubator at 37 °C, 5% CO_2 and 95% humidity for culturing. The medium was changed every two days. The passage was carried out when 80–90% of the culture dish was covered with cells. The cells of passages 3–4 were used for the following experiments.

2.3.3. *In vitro* cell biocompatibility evaluation. Live/dead, CCK-8, and EDU experiments were used to evaluate the *in vitro* biocompatibility of the scaffold to rBMSCs. The live/dead kit (Thermo Fisher Scientific, USA) was used to evaluate cell activity. First, round coverslips were placed in the 12 well culture plate. Then, 5×10^4 cells per well were seeded evenly on the plate with the scaffold extract. After being cultured for 4 days, a staining reagent was added to incubate at 37 °C for 30 minutes, and a fluorescence microscope (OLYMPUS, BX53, Japan) was used to record the images.

A CCK-8 kit (Mei5 Biotechnology, Beijing, China) was used to analyze cytotoxicity. 3×10^4 cells per well were spread on a 12-well culture plate and cultured for 1, 4, and 7 days with the extract. At each time point, CCK-8 solution was added and incubated in the dark for 1 hour, and the OD value was measured with the microplate reader (Spectra Max 190) at a wavelength of 450 nm.

An EDU-555 cell proliferation kit (Beyotime, Shanghai, China) was used to observe the proportion of proliferating cells. The six-well culture plate was inoculated with 6×10^4 cells per well. When the cells returned to their normal state, the scaffold extract of each group was added to continue the culture and incubated for 2.5 hours after adding EDU. The cells were then fixed with 4% paraformaldehyde for 15 minutes and punched with a permeabilization buffer for 12 minutes. Subsequently, the click reaction solution was added to incubate in darkness for 30 minutes. Hoechst 33342 was used to stain the nucleus. Images were recorded using an inverted fluorescence microscope (Nikon, TE2000-U, Japan), and the Image J software was used to analyze the proliferation rate.

2.3.4. Cytoskeleton observation. A six-well culture plate was seeded with 6×10^4 cells per well with the scaffold extract to culture for 72 hours. Next, all cells were fixed with 4% paraformaldehyde for 10 minutes and pretreated with Triton X-100 for 5 minutes. After cleaning with PBS, TRITC-labeled phalloidine solution (Solarbio, Beijing, China) with a final concentration of 100 nM was added to the cell surface for F-actin staining. The cell nucleus was labeled with a 4′,6-diamidino-2-phenylindole (DAPI, Solarbio, Beijing) solution for 5 minutes in the dark. F-actin was observed using an inverted fluorescence microscope, and the Image J software was used to analyze the spreading area of the cells.

2.3.5. Alkaline phosphatase (ALP) staining and activity detection. Cells at a density of 5×10^4 cells per well were seeded on a 12-well cell culture plate, and scaffold extract containing osteogenic mineralization solution was added. After 7 and 10 days of culture, a BCIP/NBT alkaline phosphatase color development kit (Beyotime, China) was used for ALP staining. Images were collected with an inverted fluorescent microscope. An alkaline phosphatase assay kit (Beyotime, China) was used for ALP activity detection. Absorbance was measured with a microplate reader at 405 nm.

2.3.6. Alizarin red staining and semi-quantification analysis. The formation of mineralized nodules in an extracellular matrix of rBMSCs was determined by adding 5×10^4 cells per well to the 12 well plate and culturing them with the scaffold extract containing osteogenic mineralized solution for 21 days. Alizarin red solution (OriCell) was added to incubate in the dark for 30 minutes. The inverted fluorescence microscope was used for Alizarin red staining. Furthermore, 10% cetylpyridinium chloride (Macklin) was used to dissolve the calcium nodules, and a microplate reader measured the OD value at a 562 nm wavelength to perform a semi-quantitative analysis.

2.3.7. Rt-qPCR analysis. Osteogenic mineralized solution and 2×10^5 cells per well were added to a six-well culture plate. After 7 days of culturing, total RNA was extracted and reverse transcribed to synthesize cDNA. The expression level of osteogenesis-related genes, including alkaline phosphatase (ALP), bone morphogenetic protein 2 (BMP-2), runt-related

Table 1 Primers used for RT-qPCR analysis

Primer	5′ to 3′ (Forward)	5′ to 3′ (Reverse)
ALP	TGATGCTCAGGACAGGAT	GGACCATAAGCGAGTTTCT
BMP2	CATCACGAAGAAGCCATC	TCATCAGTAGGGACAGAAC
RUNX2	AATGCCTCTGCTGTTATG	TTGTGAAGACCGTTATGG
VEGF	CAGCATAGCAGATGTGAATG	TTCTCCGCTCTGAACAAG
GAPDH	CCTGCACCACCAACTGCTTA	GGCCATCCACAGTCTTCTGAG

transcription factor 2 (RUNX2), and vascular endothelial growth factor (VEGF), were evaluated with Fast Green qPCR SuperMix (TransGen, China) using QuantStudio 3 (Thermo Fisher Scientific, USA). Glyceraldehyde-3-phosphate dehydrogenase (GAPDH) was used for internal reference. Synthetic primer sequences are presented in Table 1.

2.4. *In vivo* experiments

2.4.1. Construction of the critical bone defect model and porous scaffold implantation. All animal experimental schemes were performed in compliance with the policy on animal use of Kunming Medical University and approved by the Animal Experiment Ethics Review Committee of Kunming Medical University (kmmu2021268). Forty male SD rats (220–300 g body weight) were purchased from the Laboratory Animal Department of Kunming Medical University (Kunming, China) to construct the critical skull bone defect model. They were randomly divided into control, PT-1M-CN, PT-1.5M-CN, PT-1.75M-CN, and PT-2M-CN groups.

First, the SD rats were anesthetized with 1.5% pentobarbital sodium (1 mL kg^{-1}) by intraperitoneal injection. Then, the skull was exposed, and a 5 mm diameter trephine was used to establish the bone defect model. Finally, the scaffolds in each group were implanted into the defect site. The rats were subcutaneously injected with antibiotics for three consecutive days to prevent postoperative infection.

2.4.2. Micro-CT scanning and analysis. The model rats were killed with excessive anesthesia at 8 and 12 weeks to observe new bone formation, and the skull was removed and fixed in a 10% neutral formalin solution. Three-dimensional reconstruction scanning of the samples was performed using micro-CT (Scanco Medical AG, Switzerland), and parameters such as bone mineral density, bone volume, bone surface, trabecular spacing, and trabeculae thickness were measured and analyzed using CT analyzer software.

2.4.3. Histological and biosafety evaluation. After micro-CT scanning, the skull was decalcified with 10% EDTA solution. After some time, the specimens were embedded in paraffin and cut into 5 μm-thick pieces when the acupuncture had no resistance. While finding the appropriate area, the sections were stained using hematoxylin–eosin and Masson Staining Kits. After euthanasia, venous blood was collected for blood tests and the heart, lungs, liver, spleen and kidneys were removed to evaluate organ toxicity. The new bone formation in the stained sections and tissue sections was observed with a digital pathological section scanner (KFBIO).

2.5. Statistical analysis

One-way ANOVA was used for statistical analysis using GraphPad Prism software (Version 7.0). All results were expressed in mean ± SD. $P < 0.05$ was regarded as statistically significant.

3. Results and discussion

3.1. Characterization of scaffolds and Mg^{2+} release

Natural bone consists of cortical bone with less porosity in the outer layer and cancellous bone with abundant porosity in the inner layer. It has a unique porous internal network structure.[42] The porous structure of the scaffold was not only conducive to cell migration, proliferation, and osteogenic differentiation but also provided conditions for blood vessel growth, thus providing a dual guarantee for new bone formation.[43–45]

Freeze-drying technology is a common method for preparing materials with high porosity.[46,47] The SEM image shown in Fig. 1a indicates that the PT-M-CN scaffold had many interconnected pores forming a porous structure. In addition, the pore structures and porosity of PT-M-CN scaffolds are shown in Fig. 1b and c, from the mercury injection process, it can be seen that the mercury solution mainly fills the larger pores above 10 μm at the beginning of injection, and with the upregulation of pressure, smaller nano-scale pores are also injected with mercury solution, also confirmed that the pore size range of the scaffold was wider. The pore volume–pore diameter curve indicates that the pore sizes of all scaffolds were mainly concentrated between 10^4 nm and 10^5 nm. The pore size has some influence on the behavior of cells, however, the appropriate pore size of the scaffold is still unclear. The pore size of the scaffold with 300–500 μm is conducive to the growth and migration of cells, the transmission of nutrients and the growth of blood vessels, and the pore size of the scaffold with less than 300 μm is conducive to cell adhesion and osteogenic differentiation.[1,37] According to the pore diameter detection results of the scaffolds, the median pore diameter of PT-M-CN scaffold is less than 300 μm. The results showed that the PT-M-CN scaffold could be beneficial for cell adhesion and osteogenic differentiation, laying a foundation for the repair of bone defects after scaffold implantation. Table 2 shows that the PT-1.75M-CN scaffold had minimum porosity, minimum pore diameter, and maximum bulk density among the four groups of scaffolds. And the porosity of PT-M-CN scaffold is between 50% and 90%. In natural bone, the porosity of human cortical bone is 3–12%, and the porosity of cancellous bone is 50–90%.[38] Therefore, the PT-M-CN scaffold well simulates the pore structure of human cancellous bone.

From the stress–strain curve (Fig. 1d), it can be observed that the stress gradually increases with the degree of compression. It is worth noting that the structures of all the scaffolds remain intact even if the compressive strain is 80%, showing that PT-M-CN scaffolds had excellent strength and toughness. The elastic modulus of human cortical bone is 1–20 GPa, and that of cancellous bone is 2–12 MPa.[48,49] Table 3 shows that the elastic modulus of the PT-M-CN scaffold is about 1 MPa, which is close to that of cancellous bone. The mechanical properties of the scaffold are affected by porosity, and the scaffold with different porosity shows different mechanical properties. The scaffold with high porosity has lower mechanical strength, however, a scaffold with low porosity has better mechanical strength.[50] At the same time, the incorporation of Mg^{2+} will

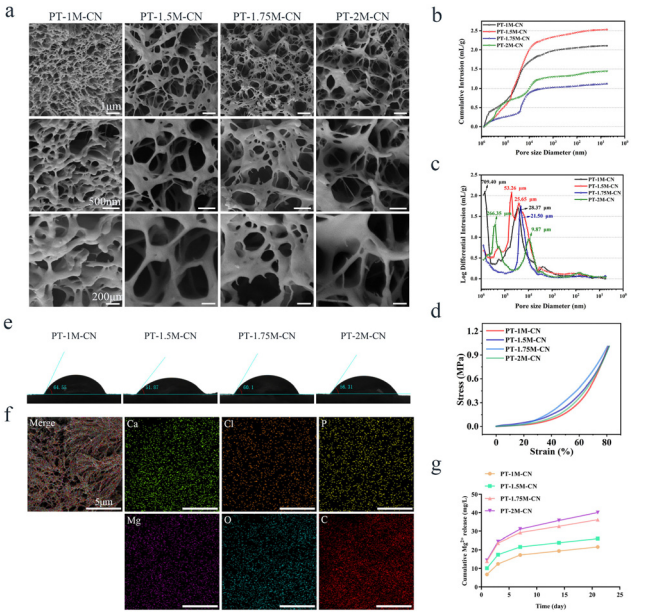

Fig. 1 (a) SEM images of the PT-M-CN scaffolds. (b) Cumulative mercury intrusion in the pore structure of the PT-M-CN scaffolds. (c) Pore volume–pore size distribution. (d) Compressive stress–strain curve of the PT-M-CN scaffolds. (e) Water contact angle of the PT-M-CN scaffolds. (f) Elemental mapping diagram of the PT-1.75M-CN scaffold. (g) Cumulative Mg^{2+} release curves at 1, 3, 7, 14, and 21 days.

Table 2 Pore characteristics of the PT-M-CN scaffolds

Sample	Porosity/%	Median pore diameter (volume)/nm	Bulk density (g mL^{-1})
PT-1M-CN	75.6808	29747.69	0.2989
PT-1.5M-CN	70.7764	37387.88	0.3359
PT-1.75M-CN	58.8009	20670.17	0.5243
PT-2M-CN	67.9121	45341.67	0.4703

lead to changes in the mechanical properties of scaffolds.[34] In combination with Tables 2 and 3, among the four groups of scaffolds prepared, the compressive strength of the scaffold gradually increases with the change of the amount of Mg^{2+} added at first, and then slowly decreases. Compared with other groups, the PT-1.75M-CN scaffold has better compressive strength, and its porosity is lower than the other three groups. And the compressive strength of the PT-M-CN scaffold is consistent with the trend of porosity. Based on the above results of the physical and chemical properties of the PT-M-CN scaffold, the PT-M-CN scaffold prepared in this study basically simulates the structure of natural human bone tissue, reaching the original design concept.

Table 3 Elastic modulus of PT-M-CN scaffolds

Sample	Elastic modulus (MPa)
PT-1M-CN	0.97628
PT-1.5M-CN	1.05333
PT-1.75M-CN	1.39377
PT-2M-CN	1.03244

The surface properties of scaffolds determine their biological effects. A hydrophilic scaffold is beneficial for cell adhesion, migration, and tissue regeneration.[51,52] The results show that the water contact angle of all scaffolds is less than 90°, indicating that the PT-M-CN scaffolds have good hydrophilicity (Fig. 1e). The elemental mapping diagram reveals that Mg^{2+} was evenly dispersed in the scaffolds (Fig. 1f). The magnesium ion release curve (Fig. 1g) shows that the Mg^{2+} in the scaffolds was gradually released over time. At 21 days, there was still a small number of magnesium ions in the extracts. This result shows that the PT-M-CN scaffolds can continuously stimulate rBMSCs to create biological effects.

3.2. *In vitro* cell experiments

3.2.1. Viability and proliferation of rBMSCs. Non-toxicity is an important prerequisite for the application of biological materials. After four days of culturing, the live/dead assay showed that the extract of the four scaffolds supported cell survival, and there was no significant difference from the control group (Fig. 2a). Different Mg^{2+} concentrations in the cell microenvironment produce different biological effects. Appropriate Mg^{2+} concentrations promote the biological effects of cells, while excessive concentrations produce cytotoxicity.[26,53–55]

As a classical method for detecting cell proliferation, it can be observed from the EDU assay results that all scaffolds promoted the proliferation of rBMSCs (Fig. 2b). According to the quantitative analysis results, the positive rate of EDU in PT-1.75M-CN was higher than that in other groups (Fig. 2c), revealing that the PT-1.75M-CN scaffold has the best ability to promote single-cell proliferation. The effect of each scaffold on cell viability was further verified by the CCK-8 assay. As shown in Fig. 2d, the results were consistent with EDU, and the OD value gradually increased with time. As mentioned above, the

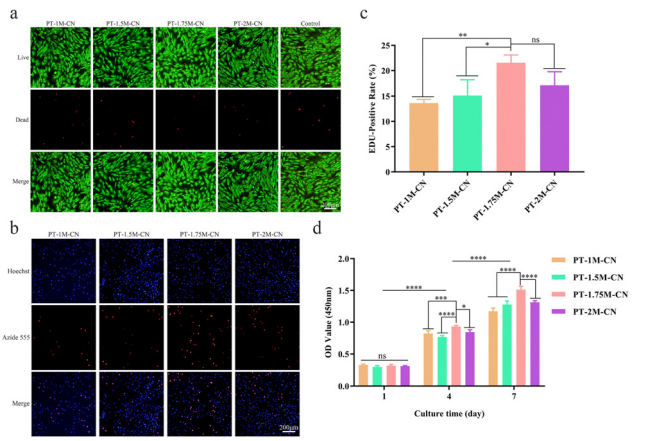

Fig. 2 (a) Live/dead staining of rBMSCs after being cultured for 4 days. Living cells are green and dead cells are red. (b) and (c) EDU single cell proliferation assay of rBMSCs. Blue represents the nucleus, and red represents EDU labeled cells. (n = 3; ns represents no significant difference; $^{*}P < 0.05$; $^{**}P < 0.01$). (d) CCK-8 assay after being cultured for 1, 4, and 7 days. (n = 5; ns represents no significant difference; $^{*}P < 0.05$; $^{***}P < 0.001$; $^{****}P < 0.0001$).

four bioactive porous scaffolds are non-toxic, biocompatible and consistent with the design concepts for medical materials.

3.2.2. F-actin expression and morphology of rBMSCs. Cell growth and development are the basic guarantees of osteogenic differentiation. In this study, the phalloidine staining results showed that the PT-M-CN bioactive porous scaffolds could stimulate rBMSCs to express F-actin (Fig. 3a). Cytoskeleton protein F-actin, an actin polymer, is the main driver of cell movement and plays an important role in cell contraction and migration. Stem cell migration is also a necessary condition for bone defect repair. Further measurements of cells typical for culturing each scaffold extract for area measurements also showed a larger cell area in the PT-1.75M-CN group (Fig. 3b and c), suggesting that it could better promote cell migration and developmental differentiation. In addition, the area spread by stem cells is potentially related to osteogenic differentiation, and a larger stem cell area increases its likelihood.[56] Therefore, the PT-M-CN scaffolds provide a basis for cell recruitment for bone defect repair.

3.2.3. Osteogenic differentiation of rBMSCs. ALP activity, calcium nodules, and osteogenesis-related gene expression levels were explored to determine the effect of PT-M-CN scaffolds on rBMSC osteogenic differentiation. As an early osteogenic marker, ALP plays an essential role in osteogenesis. As shown in Fig. 4a, there was a significant amount of ALP produced in all scaffold groups, and ALP activity gradually increased with increasing culture time (Fig. 4b). Calcium nodule formation is another sign of osteogenic differentiation. As displayed in Fig. 4c and e, many calcium nodules could be observed in each group after 21 days of culturing. The semi-quantitative results showed that the OD value of PT-1.75M-CN was significantly higher than those for other groups (Fig. 4d).

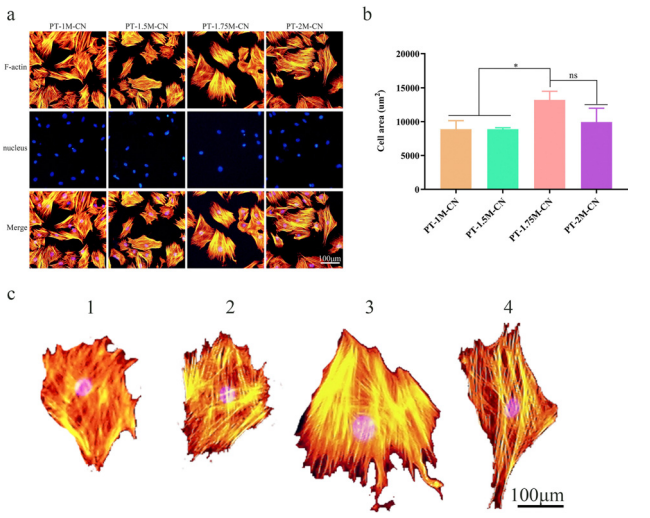

Fig. 3 (a) Morphology of rBMSCs cultured in PT-M-CN scaffold extracts. Yellow, F-actin; blue, nucleus. (b) Quantitative analysis for spreading area of rBMSCs. (n = 3; ns represents no significant difference; $^{*}P < 0.05$). (c) Representative morphology of rBMSCs in the PT-M-CN scaffold extract. 1: PT-1M-CN; 2: PT-1.5M-CN; 3: PT-1.75M-CN; 4: PT-2M-CN.

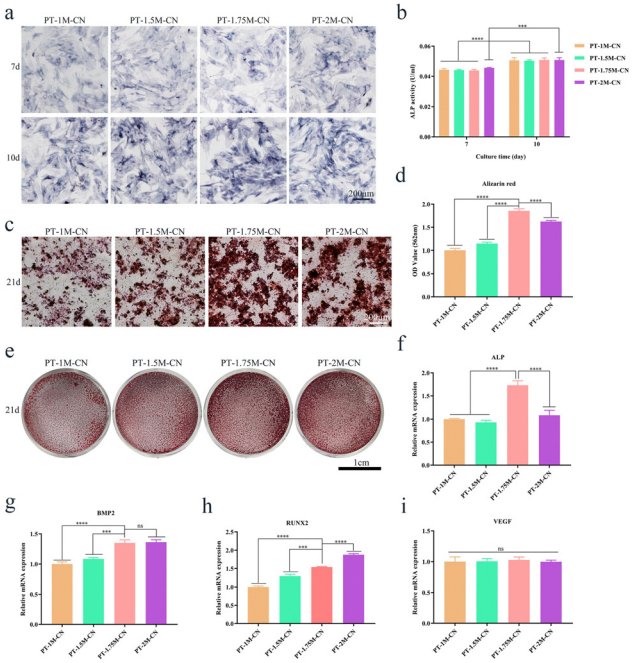

Fig. 4 (a) and (b) ALP staining and activity at 7 and 10 days. (n = 3; $^{***}P < 0.001$; $^{****}P < 0.0001$). (c)–(e) Alizarin red staining and semi-quantitative analysis at 21 days. (n = 5; $^{****}P < 0.0001$). (f)–(i) Expression level of osteogenic related genes for ALP, BMP2, RUNX2 and VEGF at 7 days. (n = 3; ns represents no significant difference; $^{***}P < 0.001$; $^{****}P < 0.0001$).

ALP, BMP2, RUNX2, and VEGF are common osteogenesis-related genes, and the Rt-qPCR assay was used to evaluate their expression levels. ALP expression in the PT-1.75M-CN group was significantly more up-regulated than in other groups after 7 days of being cultured with osteogenic induction solution (Fig. 4f). The expression of BMP2 was similar compared with the PT-2M-CN group (Fig. 4g), while the RUNX2 expression was lower in the PT-1.75M-CN group (Fig. 4h). VEGF expression was consistent in all groups (Fig. 4i). These results reveal that the PT-1.75M-CN scaffold has an enhanced ability to promote the osteogenic differentiation of rBMSCs compared with other groups. These data confirmed the correlation between the cell area and the osteogenic differentiation ability.

3.3. *In vivo* animal experiments

3.3.1. Micro-CT scanning and analysis. *In vivo* bone defect repair testing is an important practical understanding. Based on the cell experiments that verified biocompatibility, the PT-M-CN bioactive porous scaffolds were implanted in the skull defect areas of SD rats to further observe *in vivo* new bone regeneration. The skulls were removed 8–12 weeks after operation (Fig. 5).

The scaffold can serve as a "bridge" for cell migration, and osteoconductivity is also very important for the new bone formation process. Osteoconductivity of a scaffold is conducive to the migration of BMSCs and vascular endothelial cells from the edge of the bone defect to the middle defect site.[57] The

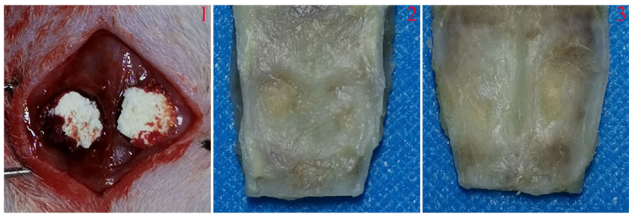

Fig. 5 Construction of critical bone defect model and porous scaffold implantation. 1: scaffold implantation; 2: aerial view of the collected sample; and 3; upward view of the collected sample.

healing of bone tissue injury includes three stages: hematoma organization stage, original callus formation stage, and callus remodeling and shaping stage. And it takes about 3 months for bone injury to reach clinical healing. Magnesium plays a vital role in bone anabolism. Normal bone metabolism means that osteoblasts and osteoclasts were in a state of dynamic balance. Calcitonin gene-related polypeptide-α (CGRP) is one of the influencing factors of bone metabolism. Previous studies have confirmed that magnesium can regulate CGRP and affect osteogenesis by promoting osteoblast proliferation and differentiation.[58,59] And it could lead to bone resorption and even lead to osteoporosis in the long term when it is lacking.

According to the micro-CT three-dimensional reconstruction and sagittal view scanning results (Fig. 6a and b), the bone defect areas were healed to a certain extent after three months of PT-M-CN scaffold implantation in SD rats. And it is apparent that the defect area in PT-1.75M-CN was smaller than that in the other groups at each time. Moreover, there were some small bone masses in the central area of the defect 12 weeks after the scaffolds were implanted, providing additional valid evidence that the scaffolds can recruit stem cells and successfully differentiate into new bone. Interestingly, new bone formation parameter analysis results were consistent, including BV/TV, BMD, BS/BV, and Tb.Th and Tb.Sp. Compared with the control and other groups, the BV/TV, BMD, and Tb.Th of the PT-1.75M-CN group were higher at 8 and 12 weeks (Fig. 6c, d and f), and the BS/BV and Tb.Sp of the PT-1.75M-CN group were smaller at each stage (Fig. 6e and g). In addition, reviewing the previous similar studies, the PT-1.75M-CN scaffold demonstrated a better bone repair effect.[60,61] All these results indicated that the PT-1.75M-CN bioactive porous scaffold was more effective at promoting bone regeneration.

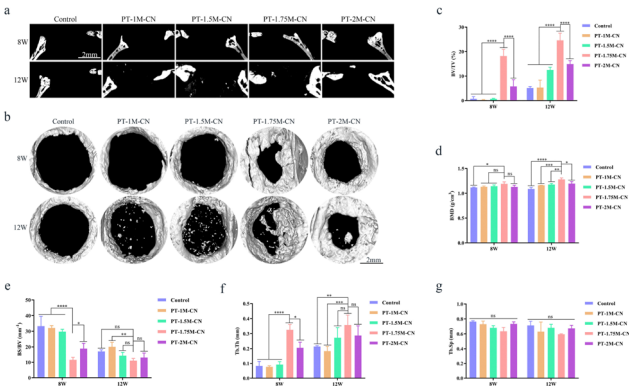

Fig. 6 Micro CT scanning and analysis of SD rat skull samples at 8 and 12 weeks after operation. (a) Sagittal view scanning of SD rat skull samples. (b) Three-dimensional reconstruction of SD rat skull samples. (c) Bone volume/total volume (BV/TV). (d) Bone mineral density (BMD). (e) Bone surface/bone volume (BS/BV). (f) Trabecular thickness (Tb.Th). (g) Trabecular Spacing (Tb.Sp). (n = 3; ns represents no significant difference; *P < 0.05; **P < 0.01; ***P < 0.001; ****P < 0.0001).

3.3.2. Histological staining. The degradability of the scaffold is another key factor of bone tissue growth, which assists the osteoinduction of the scaffold and provides favorable conditions for bone tissue regeneration.[1] The continuous degradation of bone implants can provide enough space to grow new bone tissue.[1,62,63] Matching scaffold degradation and bone regeneration rates are necessary to achieve perfect bone healing.[64] Further, bone tissue regeneration can provide follow-up guarantee for the loss of support strength due to scaffold degradation.[65]

In this study, the scaffolds in all groups degraded slowly to some extent after they were implanted for 8–12 weeks, accompanied by new bone tissue growth (Fig. 7). Among the scaffolds, the degradation rate of the PT-1.75M-CN scaffold best matched the bone defect repair process. H&E staining showed the histomorphology of scaffold groups and non-scaffold group, and no obvious inflammatory cell infiltration was found around the implant (Fig. 7a).

Masson trichrome staining further confirmed the micro-CT results. It is shown that there was only a little fibrous tissue in the defect area of the control group. At the same time, more new cartilage, cartilage matrix, and collagen fibers were formed in the scaffold group (Fig. 7b). PT-1.75M-CN showed the most significant bone regeneration, and the new bone maturity increased.

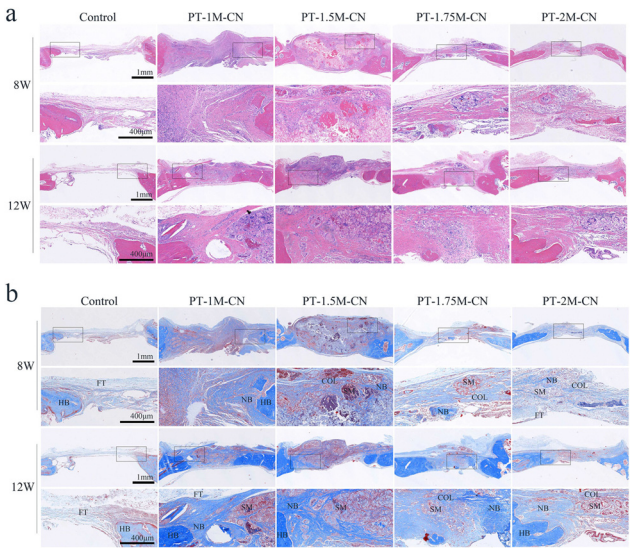

Fig. 7 (a) H&E staining. (b) Masson's trichrome staining. FT represents fiber tissue, COL represents collagenous fiber, SM represents scaffold material, NB represents new bone, and HB represents host bone.

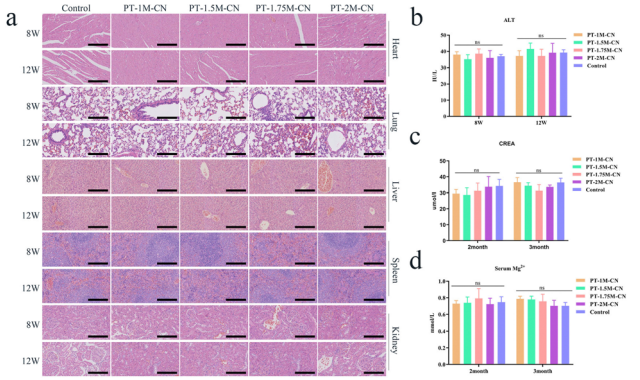

Fig. 8 (a) Histological evaluation of the heart, liver, spleen, lungs and kidneys. Scale bars are 200 μm. (b) Evaluation of liver function index. (c) Evaluation of kidney function index. (d) Serum Mg^{2+} concentration of PT-M-CN scaffolds. (ns represents no significant difference).

3.3.3. ***In vivo*** **biocompatibility evaluation.** The *in vivo* graft must be safe and harmless to tissues. Excessive concentration of Mg^{2+} released after scaffold implantation may lead to toxic effects. The safe concentration of serum magnesium toxicity *in vivo* is 5.4 mM.[66] After the PT-M-CN scaffolds were implanted for 8 and 12 weeks, *in vivo* tissue biocompatibility was evaluated with blood biochemistry and histological staining. Histological staining showed no inflammatory cell infiltration or tissue damage in important organs, including the heart, liver, spleen, lungs, and kidneys, in all scaffold groups (Fig. 8a). There was no significant difference in tissue morphology between the scaffold groups and non-scaffold group. In addition, there was no significant difference between the scaffold groups and the control group in terms of ALT, CREA, and Mg^{2+} concentrations, and the serum Mg^{2+} concentration of all scaffold groups is within the safe range (Fig. 8b–d). All the results indicated that the PT-M-CN scaffold had no damage or toxic effects on vital organs such as the liver and kidneys.

4. Conclusions

PT-M-CN porous composite scaffolds were prepared in this study using freeze-drying technology. These scaffolds effectively simulate the bone structure and composition and have high porosity and appropriate mechanical strength. *In vitro* studies showed that the scaffolds had good cell biocompatibility. Among them, the PT-1.75M-CN scaffold showed the best biological performance and could best promote cell proliferation, migration, extension, and osteogenic differentiation. *In vivo* experiments showed that the PT-1.75M-CN scaffold degraded slowly over time. New bone tissue was gradually embedded with the continuous degradation of the scaffold to better repair bone defects. In conclusion, the PT-1.75M-CN scaffold has significant potential application value as a bone substitute.

Author contributions

Zhi Shi: investigation, methodology, and writing – original draft. Guobin Huang: investigation, methodology, and formal analysis. Zhongming Li: resources. Zhenkai Lou: investigation and writing. Zhiqiang Gong: investigation and formal analysis. Xin Wang: investigation. Chengyong Li: conceptualization and writing – review & editing. Bing Wang: funding acquisition, supervision, review & editing.

Conflicts of interest

The authors declare that there is no conflict of interest in this paper.

Acknowledgements

This work was funded by the National Natural Science Foundation of China (Grant no. 82060416 and 82260449), the Major Science and Technology Project of Yunnan Provincial Department of Science and Technology, the Yunnan Provincial Orthopedic and Sports Rehabilitation Clinical Medicine Research Center (2021 02AA310068), the Yunnan Health Training Project of High-level Talents (H-2018099 and L-2018008), the Kunming Medical University Graduate Innovation Fund (2022S042) and the Yunnan Fundamental Research Projects (202101BE070001-035).

References

1 C. Xie, J. Ye, R. Liang, X. Yao, X. Wu, Y. Koh, W. Wei, X. Zhang and H. Ouyang, *Adv. Healthcare Mater.*, 2021, **10**, e2100408.
2 R. T. Annamalai, X. Hong, N. G. Schott, G. Tiruchinapally, B. Levi and J. P. Stegemann, *Biomaterials*, 2019, **208**, 32–44.
3 Z. Wang, Y. Wang, J. Yan, K. Zhang, F. Lin, L. Xiang, L. Deng, Z. Guan, W. Cui and H. Zhang, *Adv. Drug Delivery Rev.*, 2021, **174**, 504–534.
4 S. A. Ahmad Oryan, A. Moshiri and N. Maffulli, *J. Orthop. Surg. Res.*, 2014, **9**, 18.
5 M. Bahraminasab, M. Janmohammadi, S. Arab, A. Talebi, V. T. Nooshabadi, P. Koohsarian and M. S. Nourbakhsh, *ACS Biomater. Sci. Eng.*, 2021, **7**, 5397–5431.
6 S. Yin, W. Zhang, Z. Zhang and X. Jiang, *Adv. Healthcare Mater.*, 2019, **8**, e1801433.
7 N. Ramesh, S. C. Moratti and G. J. Dias, *J. Biomed. Mater. Res., Part B*, 2018, **106**, 2046–2057.
8 J. Yu, H. Xia, A. Teramoto and Q. Q. Ni, *J. Biomed. Mater. Res., Part A*, 2018, **106**, 244–254.
9 L. Xia, K. Lin, X. Jiang, B. Fang, Y. Xu, J. Liu, D. Zeng, M. Zhang, X. Zhang, J. Chang and Z. Zhang, *Biomaterials*, 2014, **35**, 8514–8527.
10 R. Wang, H. Hu, J. Guo, Q. Wang, J. Cao, H. Wang, G. Li, J. Mao, X. Zou, D. Chen and W. Tian, *J. Biomed. Nanotechnol.*, 2019, **15**, 405–415.
11 J. M. Sadowska, F. Wei, J. Guo, J. Guillem-Marti, M. P. Ginebra and Y. Xiao, *Biomaterials*, 2018, **181**, 318–332.
12 A. Soriente, I. Fasolino, A. Gomez-Sanchez, E. Prokhorov, G. G. Buonocore, G. Luna-Barcenas, L. Ambrosio and M. G. Raucci, *J. Biomed. Mater. Res., Part A*, 2022, **110**, 266–272.

13 D. Yu, W. Zhao, J. Dong, J. Zang, J. M. Regenstein, Q. Jiang and W. Xia, *Food Chem.*, 2022, **374**, 131619.
14 C. P. Jimenez-Gomez and J. A. Cecilia, *Molecules*, 2020, **25**, 3981.
15 A. Muxika, A. Etxabide, J. Uranga, P. Guerrero and K. de la Caba, *Int. J. Biol. Macromol.*, 2017, **105**, 1358–1368.
16 X. Liu, S. Zhou, B. Cai, Y. Wang, D. Deng and X. Wang, *Biomater. Sci.*, 2022, **10**, 3480–3492.
17 Y. Lu, M. Li, L. Li, S. Wei, X. Hu, X. Wang, G. Shan, Y. Zhang, H. Xia and Q. Yin, *Mater. Sci. Eng., C*, 2018, **82**, 225–233.
18 X. Zhang, L. Zhu, H. Lv, Y. Cao, Y. Liu, Y. Xu, W. Ye and J. Wang, *J. Mater. Sci.: Mater. Med.*, 2012, **23**, 1941–1949.
19 W. Wang, Q. Meng, Q. Li, J. Liu, M. Zhou, Z. Jin and K. Zhao, *Int. J. Mol. Sci.*, 2020, **21**, 487.
20 Y. Xu, S. Asghar, S. Gao, Z. Chen, L. Huang, L. Yin, Q. Ping and Y. Xiao, *Int. J. Nanomed.*, 2017, **12**, 7337–7350.
21 R. Harris, E. Lecumberri and A. Heras, *Mar. Drugs*, 2010, **8**, 1750–1762.
22 H. Y. Mi, M. R. Salick, X. Jing, B. R. Jacques, W. C. Crone, X. F. Peng and L. S. Turng, *Mater. Sci. Eng., C*, 2013, **33**, 4767–4776.
23 Z. Geng, S. Sang, S. Wang, F. Meng, Z. Li, S. Zhu, Z. Cui, Y. Jing, C. Wang and J. Su, *Biomater. Adv.*, 2022, **133**, 112647.
24 K. Bavya Devi, V. Lalzawmliana, M. Saidivya, V. Kumar, M. Roy and S. Kumar Nandi, *Chem. Rec.*, 2022, **22**, e202200136.
25 Q. Wu, S. Xu, F. Wang, B. He, X. Wang, Y. Sun, C. Ning and K. Dai, *Regener. Biomater.*, 2021, **8**, rbab016.
26 Z. Chen, W. Zhang, M. Wang, L. J. Backman and J. Chen, *ACS Biomater. Sci. Eng.*, 2022, **8**, 2321–2335.
27 W. Wang and K. W. K. Yeung, *Bioact. Mater.*, 2017, **2**, 224–247.
28 X. Jing, Q. Ding, Q. Wu, W. Su, K. Yu, Y. Su, B. Ye, Q. Gao, T. Sun and X. Guo, *Biomater. Transl.*, 2021, **2**, 197–213.
29 S. Yoshizawa, A. Brown, A. Barchowsky and C. Sfeir, *Acta Biomater.*, 2014, **10**, 2834–2842.
30 S. Zhao, K. Xie, Y. Guo, J. Tan, J. Wu, Y. Yang, P. Fu, L. Wang, W. Jiang and Y. Hao, *ACS Biomater. Sci. Eng.*, 2020, **6**, 5120–5131.
31 Y. Gu, J. Zhang, X. Zhang, G. Liang, T. Xu and W. Niu, *Tissue Eng. Regener. Med.*, 2019, **16**, 415–429.
32 X. Zhang, P. Huang, G. Jiang, M. Zhang, F. Yu, X. Dong, L. Wang, Y. Chen, W. Zhang, Y. Qi, W. Li and H. Zeng, *Mater. Sci. Eng., C*, 2021, **121**, 111868.
33 Z. Lin, D. Shen, W. Zhou, Y. Zheng, T. Kong, X. Liu, S. Wu, P. K. Chu, Y. Zhao, J. Wu, K. M. C. Cheung and K. W. K. Yeung, *Bioact. Mater.*, 2021, **6**, 2315–2330.
34 D. Qi, J. Su, S. Li, H. Zhu, L. Cheng, S. Hua, X. Yuan, J. Jiang, Z. Shu, Y. Shi and J. Xiao, *Biomater. Adv.*, 2022, **136**, 212759.
35 M. Bessa-Gonçalves, A. M. Silva, J. P. Brás, H. Helmholz, B. J. C. Luthringer-Feyerabend, R. Willumeit-Römer, M. A. Barbosa and S. G. Santos, *Acta Biomater.*, 2020, **114**, 471–484.
36 M. D. Costantino, A. Schuster, H. Helmholz, A. Meyer-Rachner, R. Willumeit-Römer and B. J. C. Luthringer-Feyerabend, *Acta Biomater.*, 2020, **101**, 598–608.
37 V. Karageorgiou and D. Kaplan, *Biomaterials*, 2005, **26**, 5474–5491.
38 H. D. Kim, S. Amirthalingam, S. L. Kim, S. S. Lee, J. Rangasamy and N. S. Hwang, *Adv. Healthcare Mater.*, 2017, **6**, 1700612.
39 M. Wang, Y. Yu, K. Dai, Z. Ma, Y. Liu, J. Wang and C. Liu, *Biomater. Sci.*, 2016, **4**, 1574–1583.
40 Y. Yu, G. Jin, Y. Xue, D. Wang, X. Liu and J. Sun, *Acta Biomater.*, 2017, **49**, 590–603.
41 C. R. Siow, P. Wan Sia Heng and L. W. Chan, *Expert Opin. Drug Delivery*, 2016, **13**, 1595–1608.
42 C. Ma, T. Du, X. Niu and Y. Fan, *Bone Res.*, 2022, **10**, 59.
43 J. E. Won, Y. S. Lee, J. H. Park, J. H. Lee, Y. S. Shin, C. H. Kim, J. C. Knowles and H. W. Kim, *Biomaterials*, 2020, **227**, 119548.
44 A. H. Alice Cheng, D. J. Cohen, B. D. Boyan and Z. Schwartz, *Biofabrication*, 2014, **6**, 045007.
45 J. A. Kim, J. Lim, R. Naren, H. S. Yun and E. K. Park, *Acta Biomater.*, 2016, **44**, 155–167.
46 C. Xie, S. Liu, Q. Zhang, H. Ma, S. Yang, Z. X. Guo, T. Qiu and X. Tuo, *ACS Nano*, 2021, **15**, 10000–10009.
47 S. Rizal, E. B. Yahya, H. P. S. Abdul Khalil, C. K. Abdullah, M. Marwan, I. Ikramullah and U. Muksin, *Gels*, 2021, **7**, 246.
48 C. Öhman, M. Baleani, C. Pani, F. Taddei, M. Alberghini, M. Viceconti and M. Manfrini, *Bone*, 2011, **49**, 769–776.
49 Ž. Perić Kačarević, P. Rider, S. Alkildani, S. Retnasingh, M. Pejakić, R. Schnettler, M. Gosau, R. Smeets, O. Jung and M. Barbeck, *Int. J. Artif. Organs*, 2020, **43**, 69–86.
50 A. Cheng, A. Humayun, D. J. Cohen, B. D. Boyan and Z. Schwartz, *Biofabrication*, 2014, **6**, 045007.
51 R. M. Visalakshan, M. N. MacGregor, S. Sasidharan, A. Ghazaryan, A. M. Mierczynska-Vasilev, S. Morsbach, V. Mailander, K. Landfester, J. D. Hayball and K. Vasilev, *ACS Appl. Mater. Interfaces*, 2019, **11**, 27615–27623.
52 J. O. Abaricia, A. H. Shah, M. Chaubal, K. M. Hotchkiss and R. Olivares-Navarrete, *Biomaterials*, 2020, **243**, 119920.
53 A. Mochizuki, C. Yahata and H. Takai, *J. Mater. Sci.: Mater. Med.*, 2016, **27**, 145.
54 J. Wang, F. Witte, T. Xi, Y. Zheng, K. Yang, Y. Yang, D. Zhao, J. Meng, Y. Li, W. Li, K. Chan and L. Qin, *Acta Biomater.*, 2015, **21**, 237–249.
55 A. Cerqueira, I. Garcia-Arnaez, M. Muriach, M. Azkargorta, F. Elortza, R. Izquierdo, F. Romero-Gavilan, M. Gurruchaga, J. Suay and I. Goni, *Biomater. Sci.*, 2022, **10**, 5634–5647.
56 F. Jiao, Y. Zhao, Q. Sun and B. Huo, *J. Biomed. Mater. Res., Part A*, 2020, **108**, 2080–2089.
57 F. E. Weber, *Tissue Eng., Part B*, 2019, **25**, 375–386.
58 M. Nabiyouni, T. Bruckner, H. Zhou, U. Gbureck and S. B. Bhaduri, *Acta Biomater.*, 2018, **66**, 23–43.
59 Y. Yan, Y. Wei, R. Yang, L. Xia, C. Zhao, B. Gao, X. Zhang, J. Fu, Q. Wang and N. Xu, *Colloids Surf., B*, 2019, **179**, 309–316.
60 Y. Lai, Y. Li, H. Cao, J. Long, X. Wang, L. Li, C. Li, Q. Jia, B. Teng, T. Tang, J. Peng, D. Eglin, M. Alini, D. W. Grijpma, G. Richards and L. Qin, *Biomaterials*, 2019, **197**, 207–219.

61 X. Chen, C. Gao, J. Jiang, Y. Wu, P. Zhu and G. Chen, *Biomed. Mater.*, 2019, **14**, 065003.
62 A. M. Maadani and E. Salahinejad, *J. Controlled Release*, 2022, **351**, 1–7.
63 D. da Silva, M. Kaduri, M. Poley, O. Adir, N. Krinsky, J. Shainsky-Roitman and A. Schroeder, *Chem. Eng. J.*, 2018, **340**, 9–14.
64 S. Naahidi, M. Jafari, M. Logan, Y. Wang, Y. Yuan, H. Bae, B. Dixon and P. Chen, *Biotechnol. Adv.*, 2017, **35**, 530–544.
65 P. Feng, P. Wu, C. Gao, Y. Yang, W. Guo, W. Yang and C. Shuai, *Adv. Sci.*, 2018, **5**, 1700817.
66 J. Long, B. Teng, W. Zhang, L. Li, M. Zhang, Y. Chen, Z. Yao, X. Meng, X. Wang, L. Qin and Y. Lai, *Biomater. Transl.*, 2021, **2**, 272–284.